INTERNATIONAL JOURNAL FOR NUMERICAL METHODS IN FLUIDS, VOL. 7, 49–67 (1987)

# NUMERICAL SIMULATION OF THE HORIZONTAL BRIDGMAN GROWTH. PART II: THREE-DIMENSIONAL FLOW

S. DUPONT, J. M. MARCHAL AND M. J. CROCHET

*Université Catholique de Louvain, Louvain-la-Neuve, Belgium*

AND

F. T. GEYLING

*Bell Laboratories, Murray Hill, New Jersey, U.S.A.*

## SUMMARY

We study the steady-state three-dimensional flow which occurs in a horizontal crucible of molten metal under the action of a horizontal temperature gradient. The geometry and the boundary conditions are similar to those encountered in the Bridgman growth process of semiconductor crystals. We find that three-dimensional effects can have a dramatic influence upon the flow, which, before the onset of periodic disturbances, differs appreciably from its two-dimensional counterpart. We also investigate the sensitivity of the flow to non-symmetric disturbances.

KEY WORDS Finite Elements Transient Flows Three-dimensional Flows Natural Convection Interfaces Oscillatory Flows Crystal Growth Semiconductors Gallium Arsenide

## 1. INTRODUCTION

In an earlier paper, Crochet, Geyling and Van Schaftingen[1] have investigated the two-dimensional time-dependent flow which occurs in a molten metal contained in a rectangular cavity subjected to a horizontal temperature gradient. Such a configuration is typical of the Bridgman crystal growth process, where it is known that thermal oscillations appear beyond a critical value of the temperature gradient. The phenomenon was well illustrated in experiments carried out by Hurle, Jakeman and Johnson[2] with a crucible of molten gallium.

Crochet, Geyling and Van Schaftingen[1] have shown that the occurrence of a periodic motion in the melt is not incompatible with the plane flow hypothesis. At fairly low values of the Grashof number, the structure of the flow in the cavity subdivides into multiple cells which eventually oscillate in size and intensity, producing at the same time a periodic temperature field. Other explanations for the onset of periodic disturbances have been proposed by Hart[3] and Gill.[4]

The subdivision of the flow structure into multiple cells is already present in the steady-state configuration, and one may wonder whether this feature is preserved in a three-dimensional flow configuration which is typical of the Bridgman growth process, i.e. where the width of the crucible is close to twice its depth. Mallinson and de Vahl Davis[5] have indeed shown that three-dimensional effects can be very important in a cavity with side heating. In the present paper, we would like to

0271-2091/87/010049-19$09.50

*Received 2 April 1986*
*Revised 25 June 1986*

investigate the nature of the three-dimensional steady state flow occurring in the crucible, and to discover whether, at that early stage of the flow, one may indeed observe multiple cells which will eventually generate the periodic motion.

We wish to pursue our investigation with the use of finite elements. Our main incentive is the development of numerical techniques for predicting the location of the liquid–solid interface during the growth process; finite elements are well suited for such a purpose. The literature on three-dimensional finite elements is, however, scarce. Although three-dimensional finite elements are widely used in structural mechanics, their development within the context of fluid mechanics has been slow. The obvious reason is the high computer cost associated with the iterations in solving non-linear problems. For our present purpose, it has been found necessary to investigate the behaviour of several finite element algorithms. A major concern in selecting a finite element is to keep a proper balance between cost and accuracy. Out of six possible elements, only two have been retained. The final selection has taken into account the fact that highly refined meshes would be prohibitive for representing the flow domain.

After a short presentation of the basic equations in section 2, we will analyse the performances of our finite elements in section 3, on the basis of a comparison with a two-dimensional solution on a highly refined mesh. In section 4, we will analyse the three-dimensional steady flow in a rectangular parallelepiped and discover that the three-dimensional flow differs sensibly from its two-dimensional counterpart. This will be further emphasized in section 5 where we exhibit trajectories of material particles.

The experimental results by Hurle, Jakeman and Johnson[2] had shown evidence of a lack of symmetry of the flow with respect to the intended longitudinal plane of symmetry. In section 6, we consider the full crucible in order to leave enough freedom for a non-symmetrical motion. Also, we introduce a slight lack of symmetry of the boundary conditions, but the flow remains essentially symmetrical.

Finally, in section 7, we consider briefly the flow in a cylindrical crucible.

## 2. BASIC EQUATIONS

We wish to calculate a three-dimensional buoyancy-driven flow in a crucible filled with molten metal. Two different shapes will be adopted for the crucible: a rectangular parallelepiped and a half cylinder with straight ends. The upper boundary is a free surface. In the Bridgman growth process, the crucible is surrounded by heating elements and the real thermal boundary conditions are fairly complex. In the present paper, we will assume that the temperature is imposed on the boundary (including the free surface) and varies linearly between the two ends. The horizontal temperature gradient creates natural convection in the crucible.

In view of the relatively narrow range of temperatures encountered in the Bridgman process, we may assume that the shear viscosity of the melt is uniform. The motion is then governed by the Navier–Stokes equations with the Boussinesq approximation for the body forces, i.e.

$$-\frac{1}{\rho_1}\nabla p + \nu\Delta\mathbf{v} + \frac{\rho}{\rho_1}\mathbf{g} = \frac{\partial\mathbf{v}}{\partial t} + \mathbf{v}\cdot\nabla\mathbf{v},$$

$$\nabla\cdot\mathbf{v} = 0, \tag{1}$$

where $p$ is the pressure, $\mathbf{v}$ the velocity field, $\mathbf{g}$ the acceleration due to gravity, $\nu$ the kinematic viscosity; $\rho_1$ is the density at the melting point, and the density $\rho$ is given by

$$\rho = \rho_1[1 - \alpha(T - T_1)], \tag{2}$$

where $T$ is the temperature and $\alpha$ the coefficient of thermal expansion. The symbols $\nabla$ and $\Delta$ denote respectively the gradient and the Laplacian operators.

The temperature field is the solution of the energy equation, which has the form

$$\frac{\partial T}{\partial t} + \mathbf{v}\cdot\nabla T = \kappa \Delta T, \tag{3}$$

where $\kappa$ is the thermal diffusivity of the melt. We assume that there are no heat sources in the melt and we neglect viscous dissipation. The present paper being devoted to the calculation of steady-state solutions, the partial derivatives with respect to time will be omitted in (1) and (3).

It is convenient to solve the problem in terms of non-dimensional variables. We select the depth $h$ of the melt as a characteristic length, the ratio $v/h$ as a characteristic velocity and the maximum temperature difference between the ends as a characteristic temperature. Then the system (1)–(3) becomes

$$\begin{aligned} -\nabla p + \Delta \mathbf{v} - Gr\, T\mathbf{e} - \mathbf{v}\cdot\nabla\mathbf{v} &= \mathbf{0}, \\ \nabla\cdot\mathbf{v} &= 0, \\ \Delta T - Pr\,\mathbf{v}\cdot\nabla T &= 0, \end{aligned} \tag{4}$$

where $\mathbf{e}$ is a unit vector orientated along the gravity field. The Grashof number $Gr$ is given by

$$Gr = \frac{\alpha(T_1 - T_0)gh^3}{v^2},$$

where $(T_1 - T_0)$ is the temperature difference between the end walls and $g$ is the acceleration due to gravity. The Prandtl number is defined by

$$Pr = v/\kappa. \tag{5}$$

The order of magnitude of $Gr$ in practical applications is $10^6$ to $10^7$. The Prandtl number of molten metals is of order of $10^{-2}$. In part I of the present series,[1] we adopted $Pr = 0{\cdot}015$ for the growth of gallium arsenide. Later physical investigations have shown that $Pr = 0{\cdot}069$ is a more appropriate value, which will be adopted in the present paper.

The system (4) will be solved by means of the finite element method. The flow domain is covered by a mesh of solid elements on which one identifies nodes and nodal values for the three velocity components, the temperature and possibly the pressure. We will use the same shape functions $\psi_i$ for the velocity and the temperature interpolation, whereas $\phi_i$ denotes the shape functions for the pressure. The finite element representation is given as follows:

$$\mathbf{v}^* = \sum \mathbf{V}^i \psi_i, \quad T^* = \sum T^i \psi_i, \quad p^* = \sum P^i \phi_i. \tag{6}$$

where $\mathbf{V}^i$, $T^i$ and $P^i$ denote the nodal values associated with the velocity components, the temperature and the pressure, respectively.

In order to calculate these nodal values, we use the Galerkin formulation of the field equations (4). More precisely, we replace the system (4) by the system

$$\begin{aligned} \langle \psi_i; \mathbf{v}^*\cdot\nabla\mathbf{v}^* \rangle + \langle \nabla\psi_i^{\mathrm{T}}; -p^*\mathbf{I} + (\nabla\mathbf{v}^* + \nabla\mathbf{v}^{*\mathrm{T}}) \rangle + \langle \psi_i; Gr\, T^*\mathbf{e} \rangle &= \mathbf{F}_i, \\ \langle \phi_i; \nabla\cdot\mathbf{v}^* \rangle &= 0, \\ \langle \psi_i; Pr\,\mathbf{v}^*\cdot\nabla T^* \rangle + \langle \nabla\psi_i^{\mathrm{T}}; \nabla T^* \rangle &= Q_i, \end{aligned} \tag{7}$$

where the brackets denote the $L^2$ scalar product, $\mathbf{I}$ is the unit vector, $\mathbf{F}_i$ is nodal force and $Q_i$ is the

nodal flux corresponding to the $i$th node on the boundary. The non-linear algebraic system in the nodal values $\mathbf{V}^i$, $T^i$ and $P^i$ is solved by successive increments of $Gr$ coupled with Newton–Raphson iterations.

Since the iterative procedure can be very costly for solving non-linear three-dimensional flows, special care is needed for selecting the shape functions $\psi_i$ and $\phi_i$ in (6).

## 3. CHOICE OF A FINITE ELEMENT

The problem to be solved here is truly three-dimensional, in the sense that the flow cannot be considered insensitive to the width of the crucible. The solution of three-dimensional coupled problems is very expensive in computer time, and the choice of a finite element algorithm must result from a compromise between precision and economy. For choosing the most appropriate element, we have compared six different algorithms and studied their behaviour in the solution of a two-dimensional problem which is representative of the three-dimensional problems to be solved at a later stage.

The three finite elements that we have used are shown in Figure 1: element (a) is the classical eight-node Lagrangian or serendipity element, element (b) is the twenty-node serendipity element and element (c) is the Lagrangian twenty-seven-node element. With element (a), trilinear shape functions have been used for interpolating the velocity components and the temperature between the nodes, whereas (quadratic) serendipity and triquadratic shape functions have been adopted with elements (b) and (c), respectively. In taking care of the incompressibility constraint, we have explored two different approaches. In the first approach, the pressure is made explicit, and its interpolation is given by means of polynomials which have one degree less than the polynomials used for interpolating the velocity field; a constant pressure is used with element (a), whereas trilinear shape functions are adopted with (b) and (c). In the second approach, we have used the penalty formulation in which the pressure is given a constitutive equation, i.e.

$$p = -\lambda \nabla \cdot \mathbf{v}, \tag{8}$$

and the right-hand side of (8) is substituted for $p$ in (1). The procedure requires the use of reduced integration for the calculation of the stiffness matrix. The natures of the six elements are summarized in Table I.

The six elements have been tried on a typical two-dimensional problem shown in Figure 2; the geometry corresponds to a $2 \times 1$ container with a free surface on top. The fluid does not slip along the bottom and the side walls, and the temperature on the boundary is a linear function of the horizontal co-ordinate. For the test problem, $Pr = 0{\cdot}069$ and $Gr = 750{,}000$; the value of $Gr$ is low

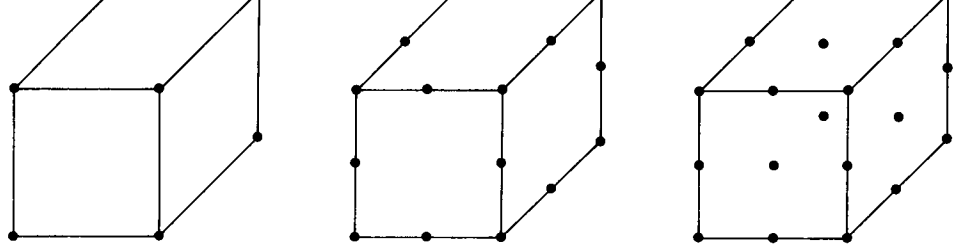


Figure 1. Three-dimensional elements: (a) eight-node brick element, (b) twenty-node serendipity element, (c) twenty-seven-node Lagrangian element

Table I. Finite elements used for the comparison

| Element | Velocity and temperature interpolation | Pressure interpolation | Result |
|---|---|---|---|
| I | Trilinear | Constant | Pressure modes |
| II | Trilinear | Penalty | |
| III | Serendipity quadratic | Trilinear | Vanishing pivot |
| IV | Serendipity quadratic | Penalty | Inaccurate |
| V | Triquadratic | Trilinear | |
| VI | Triquadratic | Penalty | Ill-Conditioned |

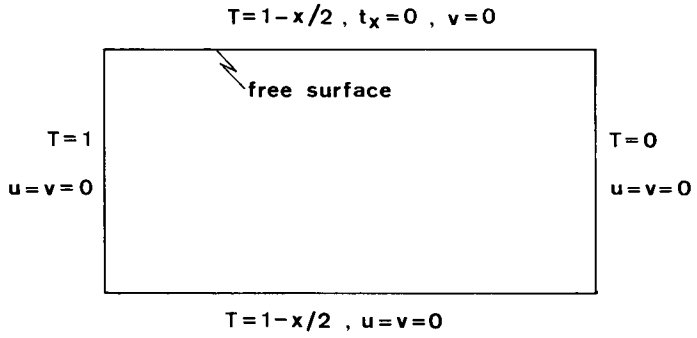


Figure 2. Geometry and boundary conditions of the test problem

enough to ensure the existence of a steady-state solution. A reference solution has been obtained by means of a two-dimensional program using Lagrangian elements with biquadratic shape functions for the velocity components and the temperature and bilinear shape functions for the pressure. The mesh for the reference solution is very dense; it contains 38 × 20 elements and 3157 nodes (10,290 variables). For studying the behaviour of trilinear shape functions, we have adopted a mesh of 19 × 10 elements; for triquadratic and serendipity elements, the mesh contains 9 × 5 elements so that all meshes have essentially the same number of nodes.

Problems are encountered with four of the six elements. Element I gives rise to chequerboard pressure modes.[6] A zero pivot occurs during the Gaussian elimination with element III (with diagonal pivoting), and the convergence properties of the iterative process with element VI were so poor that we could not reach a value of *Gr* higher than 10,000. The solution obtained with element IV deviates too much from the reference solution, and this confirms the superiority of Lagrangian elements over serendipity elements in convective problems. The axial velocity profile on the free surface obtained with element IV is compared to the reference solution in Figure 3, together with the results of elements II and V. We are thus left with elements II and V. The mathematical theory of finite elements shows that element V has a faster rate of convergence than element II. However, our calculations show that, within a range of economically acceptable meshes, using element II leads to significant economy in computer time. Throughout the rest of the paper we will use element II of Table I.

## 4. NATURAL CONVECTION IN A RECTANGULAR CRUCIBLE

We wish to compare the three-dimensional flow taking place in a rectangular parallelepiped to the two-dimensional approximation which consists of calculating a two-dimensional flow in the plane

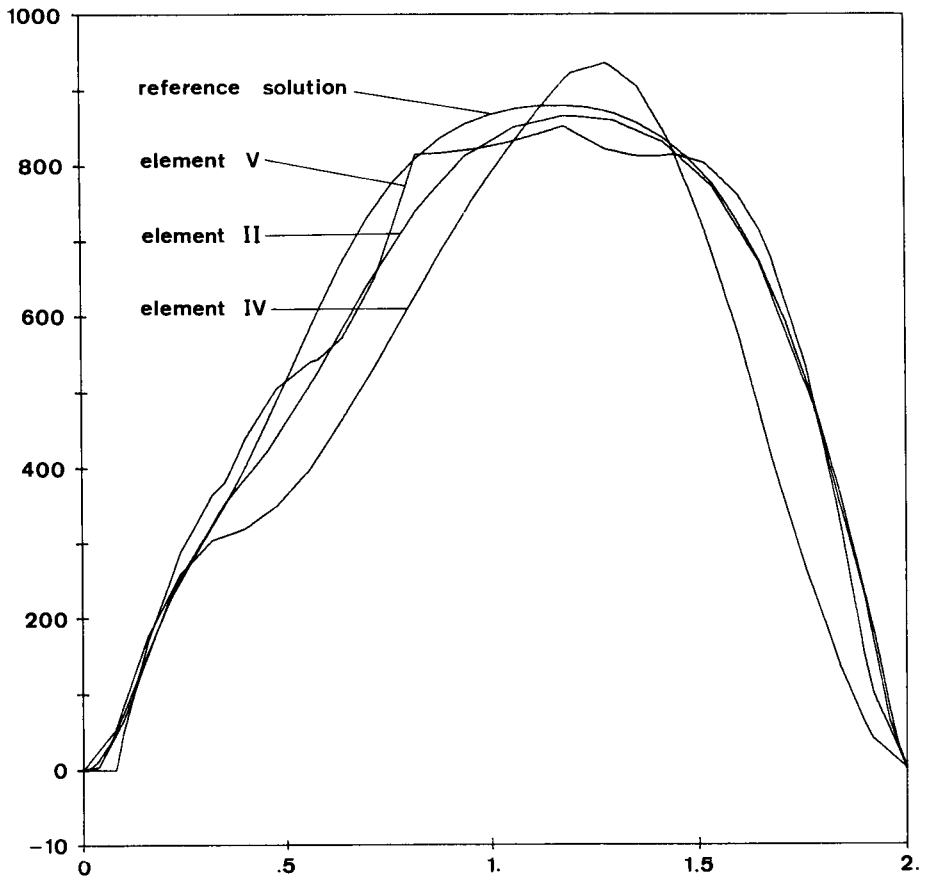


Figure 3. Horizontal velocity profile on the free surface

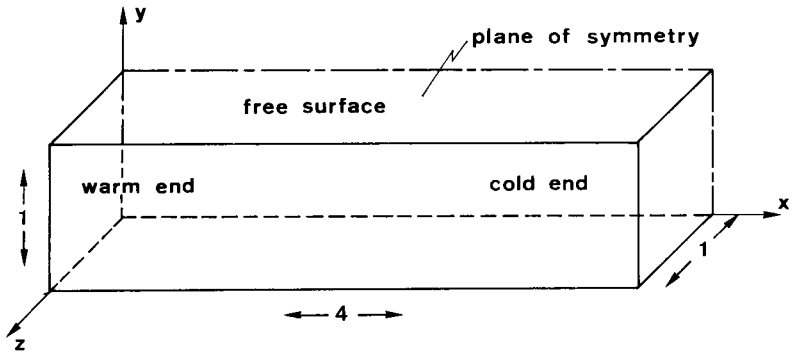


Figure 4. Geometry of the rectangular crucible

of symmetry. The geometry of the problem is shown in Figure 4. The crucible has a unit depth, a width equal to twice its depth, and a length equal to four times its depth, but in this section we will assume that there is a plane of symmetry. The (non-dimensional) temperature is 1 on the left wall and 0 on the right wall; the temperature on the longitudinal boundaries decreases linearly between the ends. The melt does not slip along the walls; however, the tangential contact forces vanish on the free surface and on the plane of symmetry.

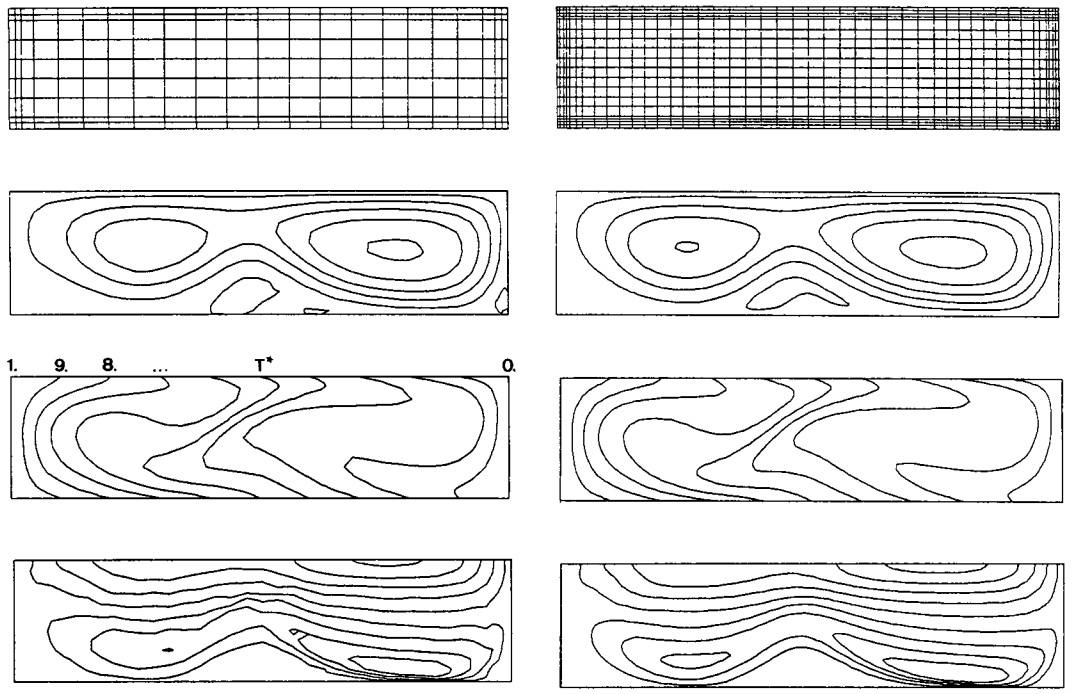


Figure 5. Results of the plane problem with $Gr = 710{,}000$: finite element mesh, streamlines, isotherms and contour lines of the horizontal velocity component. On the left: coarse mesh; on the right, refind mesh

Let us first study the corresponding two-dimensional problem. With $Pr = 0{\cdot}069$, a steady-state solution is found up to $Gr = 710{,}000$. In our earlier work, we found that the lack of convergence of the steady-state algorithm coincides in general with the onset of periodic temperature and velocity oscillations in the melt. For verifying the convergence of the two-dimensional solution we have used two meshes shown in Figure 5. The coarse mesh (2D1) contains 198 elements, 855 nodes and 2795 variables; the finer mesh (2D2) contains 792 elements, 3293 nodes and 10,734 variables. Both gave the same limiting Grashof number. In Figure 5, we show characteristic results for both meshes, i.e. the streamlines, the isotherms and contour lines of the horizontal velocity component, for the limiting value of the Grashof number ($Gr = 710{,}000$). Let us first observe that the convergence is good; the contour lines are essentially the same on both sides of the Figure. As we might expect, the contour lines are smoother with the finer mesh. Figure 5 shows the typical features of such flows in a $4 \times 1$ crucible. The flow contains two main eddies separated at the bottom by a third eddy (which grows and decays in the oscillatory flow occurring beyond the critical value of $Gr$). The isotherms are dramatically distorted by heat convection, despite the fact that an essential boundary condition is imposed on the upper and lower boundaries. Finally, the contour lines of the axial velocity component (directed from the warm wall towards the cold wall) show that it attains its maximum on the free surface near the cold end and that the flow is very slow in the small eddy at the bottom of the crucible.

Let us now consider the three-dimensional problem described in Figure 4. Again, for testing the validity of our numerical results, we have considered two finite element meshes. The coarse mesh (3D1) contains $32 \times 10 \times 9 = 2880$ elements, with 3630 nodes and 14,520 variables; the refined mesh (3D2) contains $40 \times 14 \times 10 = 5600$ elements, with 6765 nodes and 27,060 variables. Although the number of eight-node bricks along each side is not especially large, we observe that

the number of variables has already reached the impressive number of 27,060. A perspective view of the mesh 3D2 is shown in Figure 6.

The critical values of the Grashof number beyond which the iterative procedure would not converge are different for meshes 3D1 and 3D2. The value is 300,000 with the coarse mesh and 500,000 with the refined mesh, to be compared with 710,000 in the plane problem. We have not yet investigated the meaning of the limit value of $Gr$ in three-dimensional flows; such a study will require the use of a transient (and more expensive) algorithm. We will now consider separately three values of $Gr$ and compare the two-dimensional to the three-dimensional results.

Figure 7 compares the axial velocity profiles on the free surface (at the intersection of the free surface and the plane of symmetry) obtained with the two-dimensional solution and the three-dimensional solution on 3D2 at a value of $Gr = 100{,}000$. The two maxima of the curve

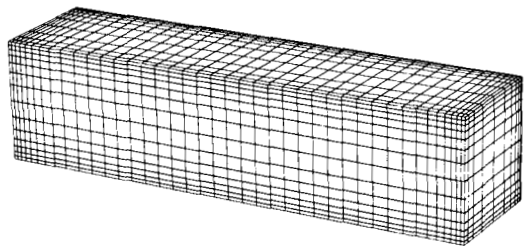

Figure 6. Perspective view of the three-dimensional finite element mesh 3D2 containing 5600 elements

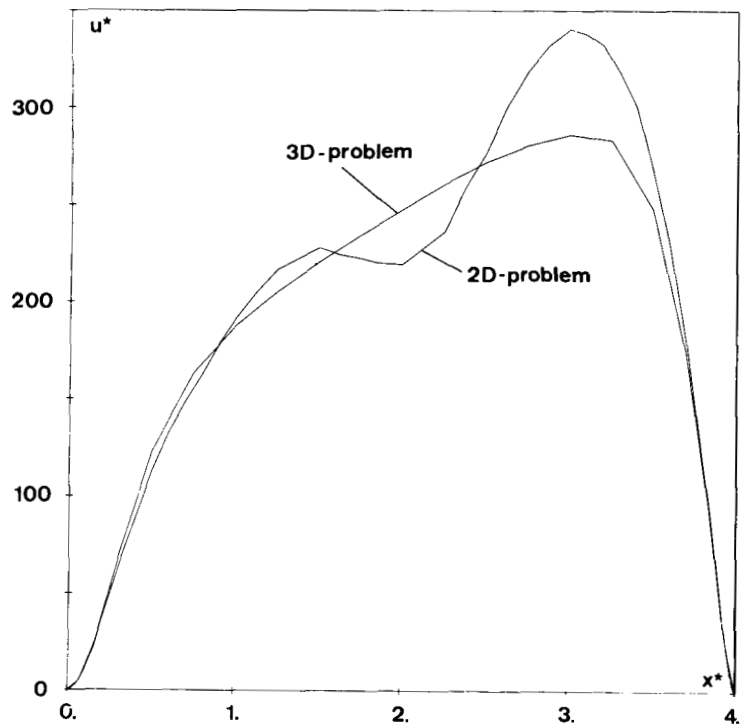


Figure 7. Axial velocity profiles on the axis of symmetry of the free surface, obtained from the two-dimensional and three-dimensional solutions on the mesh 3D2; $Gr = 100{,}000$

corresponding to a two-dimensional calculation exhibit the fact that the three-cell configuration is already present at that value of $Gr$. The curve arising from the three-dimensional solution shows only one maximum, and the structure of the flow must obviously be different. We may already have some idea of the complexity of the flow by inspection of Figure 8 which shows a perspective view of the horizontal velocity component on the free surface. One finds that the no-slip condition on the side-wall gives rise to a steep velocity gradient near it. Moreover, we observe that the horizontal velocity component is negative in the corner of the crucible at the cold end; this is the sign of a horizontal recirculation which will be confirmed at higher values of $Gr$.

Let us now analyse the flow for $Gr = 300{,}000$, which is the maximum value for which a solution has been found with the coarser mesh 3D1. Figure 9 shows the axial velocity profiles on the axis of symmetry of the free surface obtained from the two-dimensional solution and the three-dimensional solutions on the meshes 3D1 and 3D2. Two remarks must be made about Figure 9: (i) we find again a significant difference between two and three dimensions, which will be confirmed by other Figures; (ii) the curves obtained with the coarse and fine meshes do not differ sensibly, and the results obtained on the basis of 3D2 are trustworthy. The difference between the two-dimensional and the three-dimensional approaches is even more striking once we analyse the results in the plane of symmetry. The first column in Figure 10 shows the streamlines, the velocity vectors and the isotherms for the two-dimensional case. In a three-dimensional flow, it will in general be impossible to calculate a stream function in the plane of symmetry. Thus, in the second column of Figure 10, we shown the intersection of the three-dimensional meshes with the plane of symmetry, the velocity vectors in that plane and the isotherms. It is now evident that the three-dimensional flow differs appreciably from its two-dimensional counterpart. Whereas the two-dimensional flow exhibits

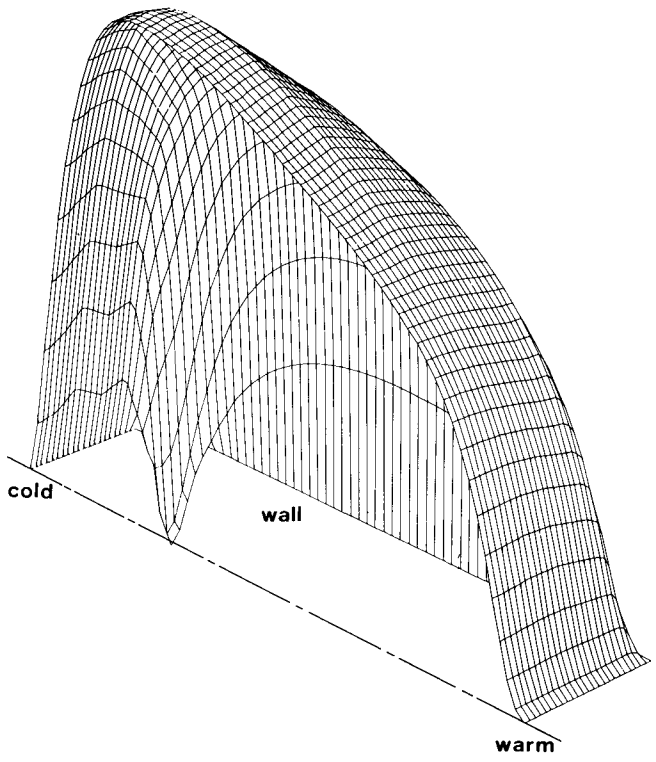


Figure 8. Perspective view of the horizontal velocity component in the $x$-direction on the free surface; $Gr = 100{,}000$

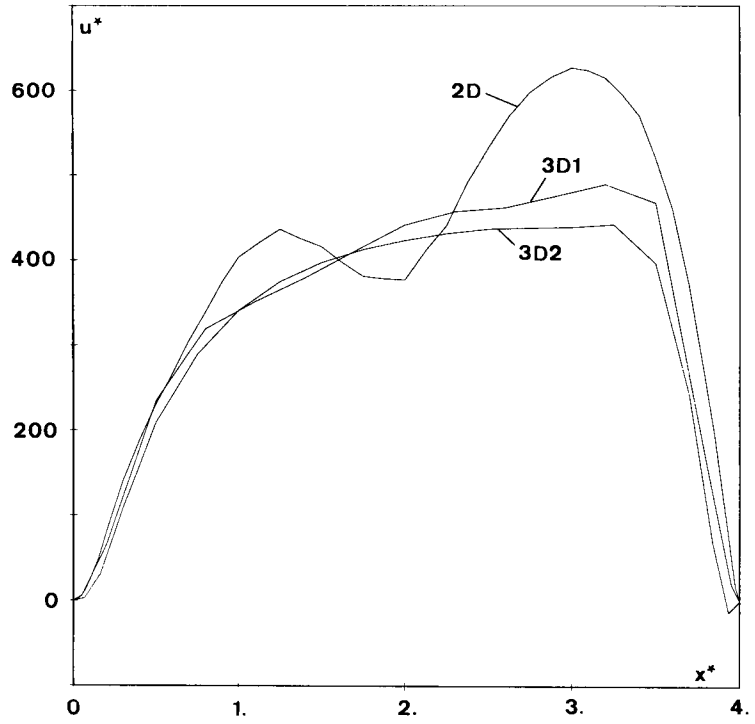


Figure 9. Axial velocity profiles on the axis of symmetry of the free surface, obtained from the two-dimensional and three-dimensional solutions; $Gr = 300{,}000$

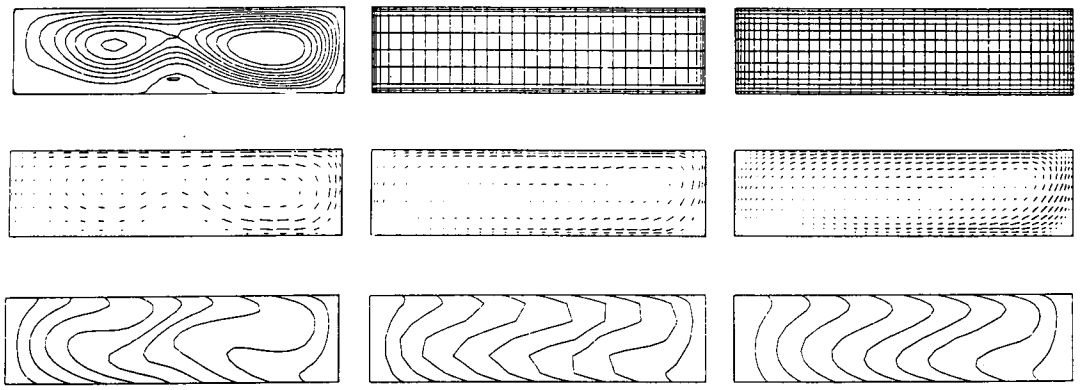

Figure 10. Streamlines (in the two-dimensional flow), velocity vectors and isotherms at $Gr = 300{,}000$: (a) in two dimensions, (b) in three dimensions with mesh 3D1, (c) in three dimensions with mesh 3D2

three typical eddies, there is only a single large convective roll in the plane of symmetry of the three-dimensional flow. However, since the horizontal velocity component has essentially the same order of magnitude in both cases, the isotherms are quite similar. From Figure 10 we may also check the convergence of the finite elements; the roughness of some curves obtained with 3D1 may be related to the fact that the iterative procedure fails to converge beyond the present value of $Gr$.

The nature of the three-dimensional flow on the free surface may be analysed in Figure 11, which shows the intersection of the mesh with the free surface, the velocity vectors (a stream function does

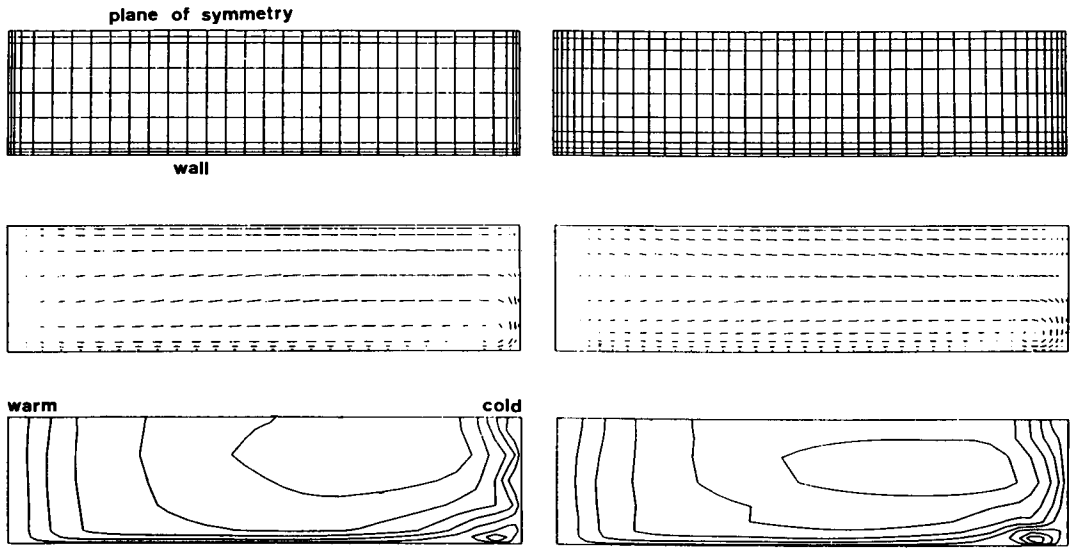


Figure 11. Finite element mesh, velocity vectors and contour lines of the axial velocity component on the free surface at $Gr = 300{,}000$ obtained with meshes 3D1 and 3D2

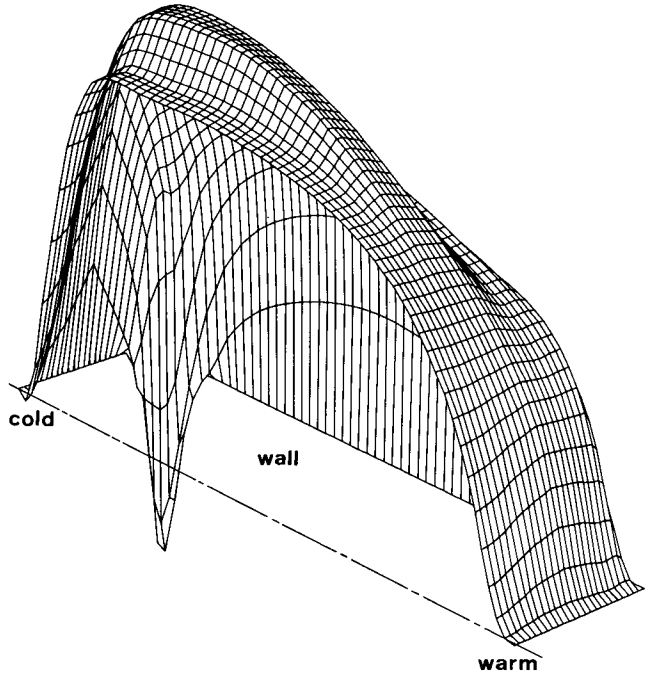


Figure 12. Perspective view of the horizontal velocity component in the $x$-direction on the free surface with mesh 3D2; $Gr = 300{,}000$

not exist) and the contour lines of the axial velocity component. We observe in Figure 11 that the flow is definitely three-dimensional in some parts of the domain. In the corner next to the cold end, one finds a recirculating region. Another interesting feature shown in Figure 11 is the fact that the axial velocity component does not reach a maximum on the axis of symmetry in all cross-sections. This is well evidenced by Figure 12 which shows a perspective view of the horizontal velocity

component on the free surface, where we can also observe the region where the velocity component changes sign.

Finally, we need to answer the question whether the temperature field varies in the lateral direction. We cannot detect the answer on the free suface since the temperature is fixed on that part of the boundary and therefore we examine the flow at mid-height between the bottom and the free surface. In Figure 13, we show the velocity vectors and the isotherms in that plane. The velocity vectors show quite well a recirculating region in the cold corner, and the isotherms exhibit dramatic three-dimensional features.

For $Gr = 500{,}000$, we compare results from mesh 3D2 with the two-dimensional results. They confirm the remarks made for $Gr = 300{,}000$. Although the two-dimensional problem reveals multiple cells, the flow in the plane of symmetry remains unicellular in the three-dimensional case. Figure 14 shows a perspective view of the axial velocity component on the free surface. We observe

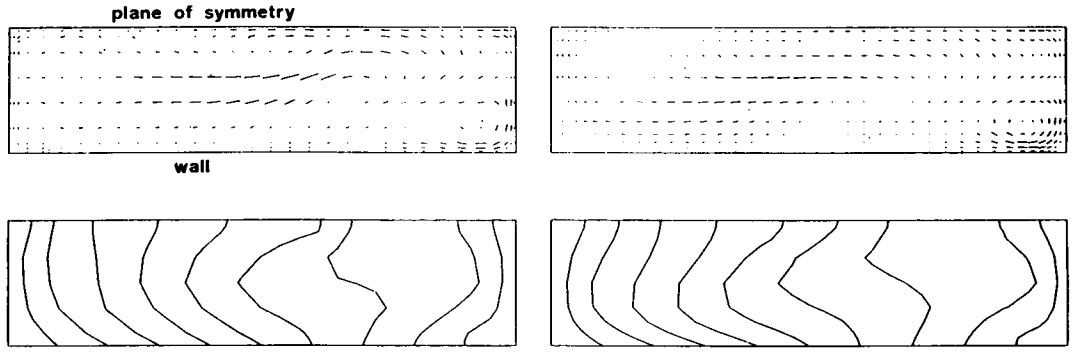


Figure 13. Velocity vectors and isotherms in a horizontal plane at mid-height at $Gr = 300{,}000$ obtained with meshes 3D1 and 3D2

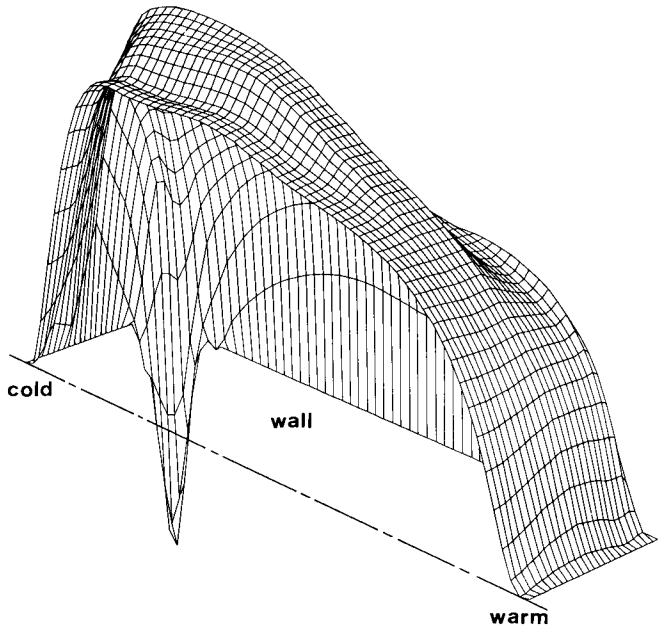


Figure 14. Perspective view of the horizontal velocity component in the $x$-direction on the free surface; $Gr = 500{,}000$

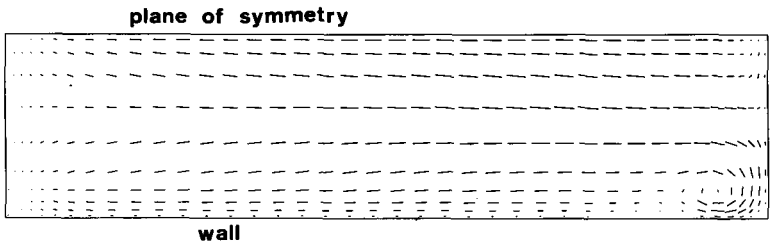


Figure 15. Velocity vectors on the free surface; $Gr = 500{,}000$

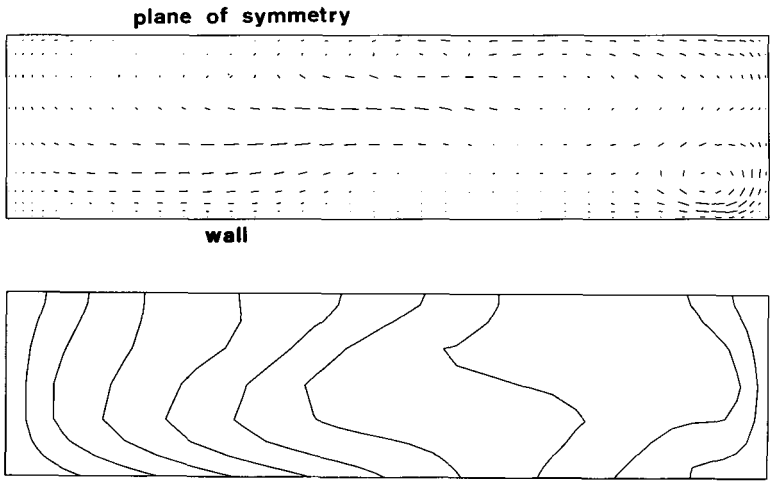


Figure 16. Velocity vectors and isotherms in a horizontal plane at mid-height at $Gr = 500{,}000$ obtained with mesh 3D2

again that the natural boundary condition is well satisfied on the plane of symmetry, that the velocity component is negative near the cold corners and that its maximum in the cross-sectional profiles does not occur on the plane of symmetry. A plot of the velocity vectors on the free surface is shown in Figure 15. The three-dimensional character of the flow is confirmed in Figure 16 which shows the velocity vectors and the isotherms in a horizontal plane located at mid-height of the crucible. The velocity vectors are obviously not aligned along the plane of symmetry and the isotherms show considerable distortion in $z$-direction.

It should be added here that the isotherm maps and the basically unicellular flow that they imply are in accord with the experimental observations of Hurle, Jakeman and Johnson.[2]

## 5. TRAJECTORIES IN A RECTANGULAR CRUCIBLE

The analysis of section 4 reveals important differences between the three-dimensional flow in a rectangular crucible and its two-dimensional counterpart. The three-dimensional character of the flow is very complex, and it is not easy to form an intuitive picture of what happens in the flow. A useful visualization is to generate the trajectory of a material particle as a function of time in the crucible.

Let $\mathbf{x}$ denote the position at time $t$ of a material particle which occupies the location $\mathbf{x}^0$ when $t = 0$. We need to solve the set of differential equations

$$\frac{d\mathbf{x}}{dt} = \mathbf{v}(\mathbf{x}), \quad \mathbf{x}(0) = \mathbf{x}^0 \tag{9}$$

The calculation is not trivial when the mesh is made of three-dimensional finite elements; indeed, for each value of **x**, one needs to find the element which contains **x** and the velocity vector at that point. The problem is much easier however with the mesh of Figure 6 made of rectangular bricks. The system (9) is solved by means of a second-order Runge–Kutta algorithm with a constant time step. The latter was selected in such a way that halving it did not alter the trajectories in a significant way.

Trajectories have been calculated with the solution at $Gr = 300{,}000$ on the refined mesh 3D2, which has been found in section 4 to give smooth results. Let us first consider a point such that $x^0 = 0{\cdot}2$, $y^0 = 0{\cdot}9$ and $z^0 = 0{\cdot}5$. Referring to Figure 4, we find that the value of $\mathbf{x}^0$ is such that the initial location is near the warm wall, near the free surface and at mid-distance between the lateral wall and the plane of symmetry. Figure 17 shows two perspective views of the trajectory of the particle

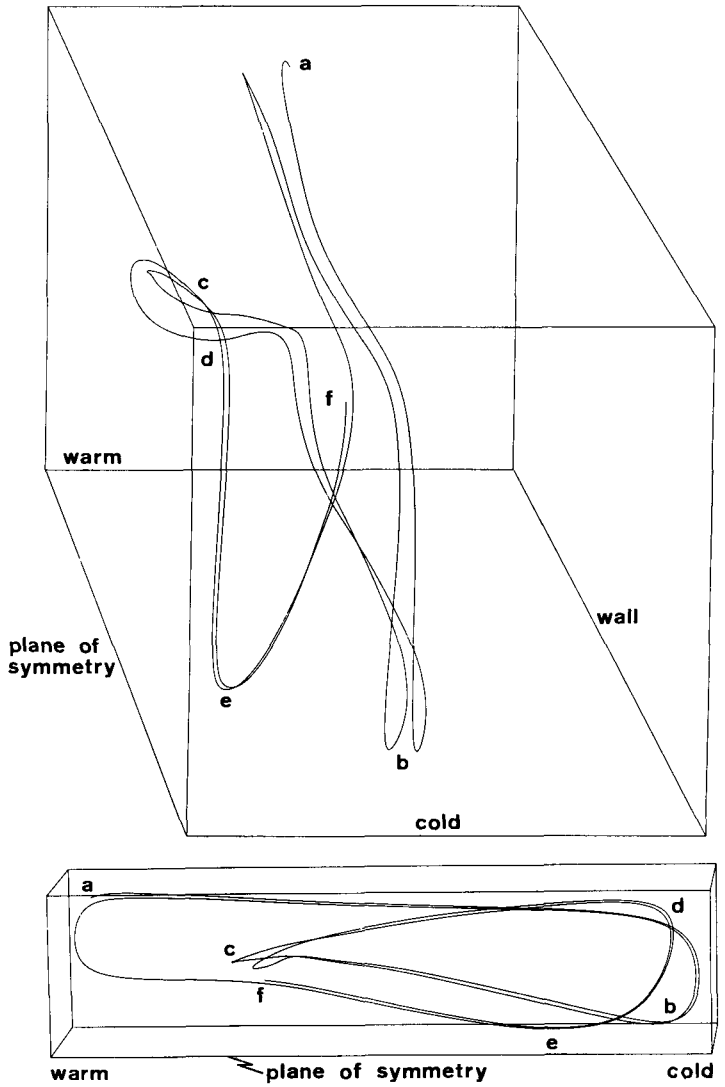


Figure 17. Perspective views of the trajectory of a particle with an initial position given by $x^0 = 0{\cdot}2$, $y^0 = 0{\cdot}9$ and $z^0 = 0{\cdot}5$. Mesh 3D2; $Gr = 300{,}000$

from a to f. Its motion is quite complex: the particle is carried towards the cold end, descends along the cold wall, is deflected towards the plane of symmetry and after a second descent along the cold wall returns to its original position.

Next, we consider a particle with an initial location given by $x^0 = 1$, $y^0 = 0{\cdot}8$ and $z^0 = 0{\cdot}1$, which is at a unit distance from the warm side, near the free surface and near the plane of symmetry. Figure 18 shows two perspective views of the trajectory of the particle which exhibit a considerable deviation with respect to plane flow. The global motion is that of a convective cell; however, a particle which descends along the cold wall near the plane of symmetry reappears on the warm wall near the outer surface.

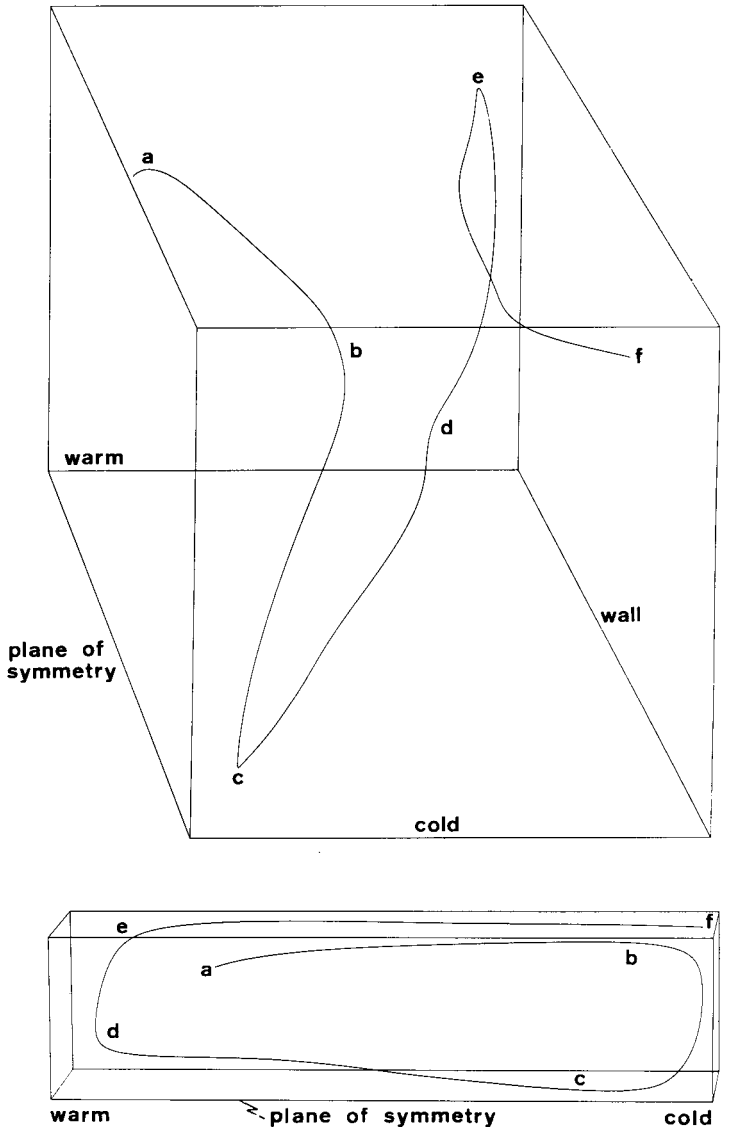


Figure 18. Perspective views of the trajectory of a particle with an initial position given by $x^0 = 1$, $y^0 = 0{\cdot}8$ and $z^0 = 0{\cdot}1$. Mesh 3D2, $Gr = 300{,}000$

## 6. NON-SYMMETRIC EFFECTS IN A RECTANGULAR CRUCIBLE

Experiments by Hurle, Jakeman and Johnson[2] on a rectangular crucible of molten gallium have exhibited isotherms which were obviously not symmetric with respect to the geometrical plane of symmetry. In section 4, we have assumed at the outset that the velocity field is symmetric, and the domain of integration consisted of one half of the rectangular crucible. In this section, we wish to consider briefly the flow in the complete crucible and allow the finite element program to generate non-symmetric solutions. In order to approach more closely the physical boundary conditions imposed by Hurle, Jakeman and Johnson we will assume that the temperature is fixed on the end walls and that the heat flux vanishes on the side walls and on the free surface. The mesh refinement adopted for the present calculations is similar to the refinement found with mesh 3D1. The mesh is shown in Figure 19; it contains 5600 elements, 6765 nodes and 27,060 variables.

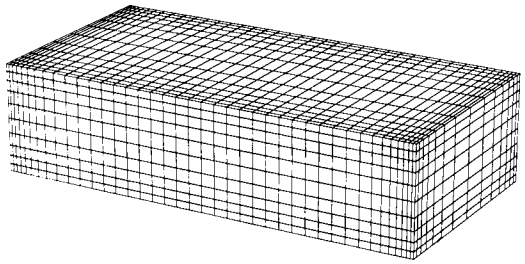

Figure 19. Perspective view of the finite element mesh used for representing the entire crucible

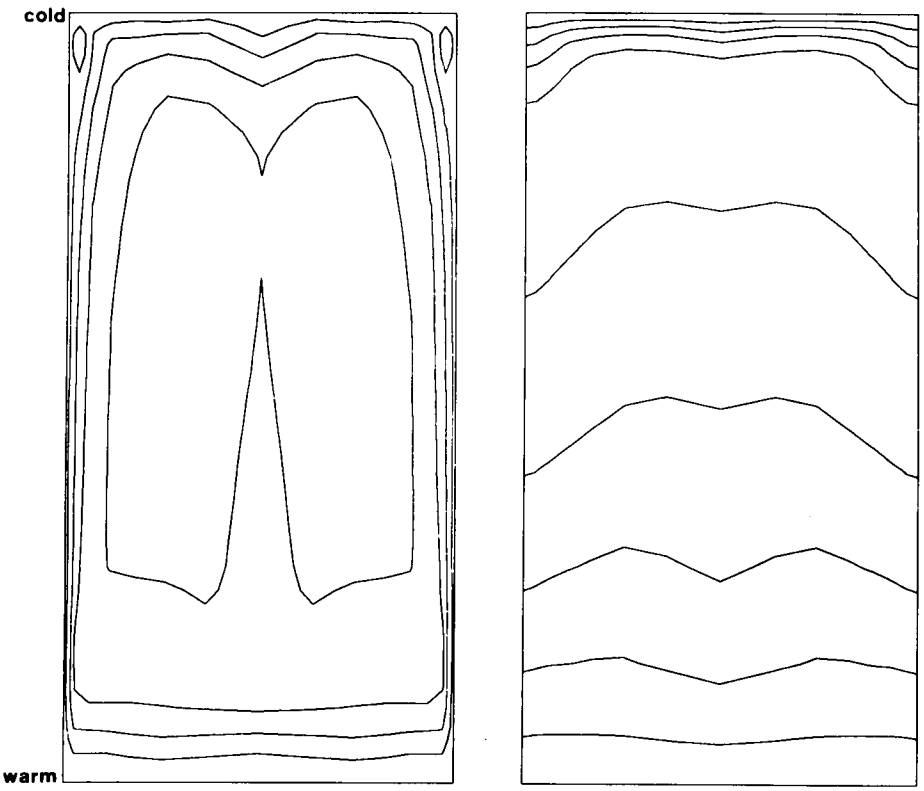


Figure 20. Contour lines of the axial velocity component and of the temperature on the free surface

Converged solutions have been obtained up to $Gr = 500{,}000$, and they do not exhibit any lack of symmetry. Figure 20 shows contour lines of the axial velocity component on the free surface; the contour lines are perfectly symmetric. Also in Figure 20, we show a plot of the isotherms on the free surface (a vanishing heat flux is imposed on all sides); one sees clearly the effect of the maximum velocity component being located away from the plane of symmetry. The flow within the plane of symmetry is unicellular and is essentially similar to that found in section 4.

Another numerical test consisted in imposing on the end walls a temperature profile which varied slightly with the $z$-co-ordinate and was not symmetric with respect to the geometrical plane of symmetry. The deviation of the numerical solution with respect to the symmetric case was of the same order of magnitude as the lack of symmetry in the boundary conditions.

## 7. THREE-DIMENSIONAL FLOW IN A CYLINDRICAL CRUCIBLE

The three-dimensional analysis of the previous sections can also be used for calculating the flow in a cylindrical crucible made of half a quartz tube. We assume that the solution is symmetric with respect to the vertical plane of symmetry of the crucible. The finite element mesh used for that purpose is shown in Figure 21; it contains 3080 elements, 3813 nodes and 15,252 variables. As in section 4, we have imposed a fixed temperature on the end walls and a linearly varying temperature field on the side walls and on the plane of symmetry. Converged solutions have been found for

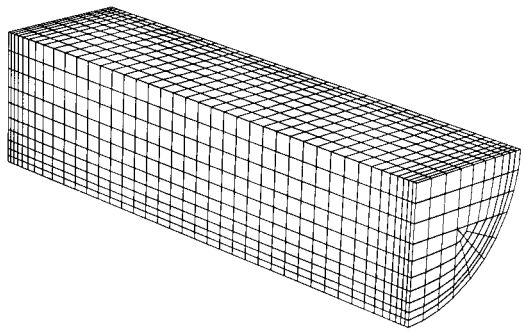

Figure 21. Finite element mesh for calculating the flow in a cylindrical crucible

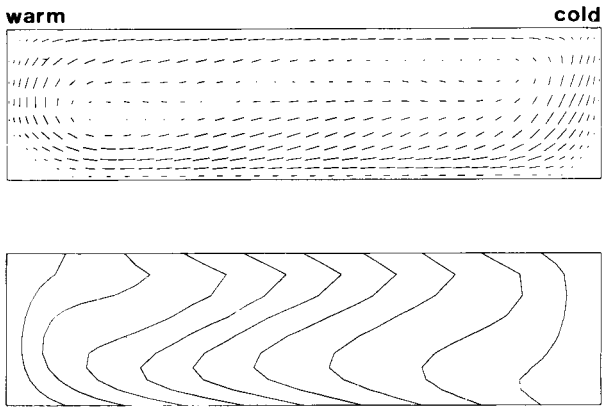


Figure 22. Velocity vectors and isotherms in the plane of symmetry; cylindrical crucible at $Gr = 300{,}000$

values up to $Gr = 550{,}000$, i.e. slightly higher than for a rectangular crucible. We will show representative results of the solution for $Gr = 300{,}000$.

Figure 22 shows a plot of the velocity vectors and the isotherms in the plane of symmetry. Once again we observe that the side walls inhibit the generation of multiple vortices; the flow in the plane of symmetry contains a single cell. We note the large value of the axial velocity at the bottom of the crucible, which is related to the fact that its width decreases with depth. The isotherms in the plane of symmetry, also shown in Figure 22, exhibit the usual configuration; they should be compared with the plots of Figure 10.

Figure 23 shows a plot of the velocity vectors on the free surface and a perspective view of the axial velocity component. Again we find a recirculating region near the cold wall. Also, we notice that the maximum of the axial velocity is reached at some distance from the plane of symmetry and

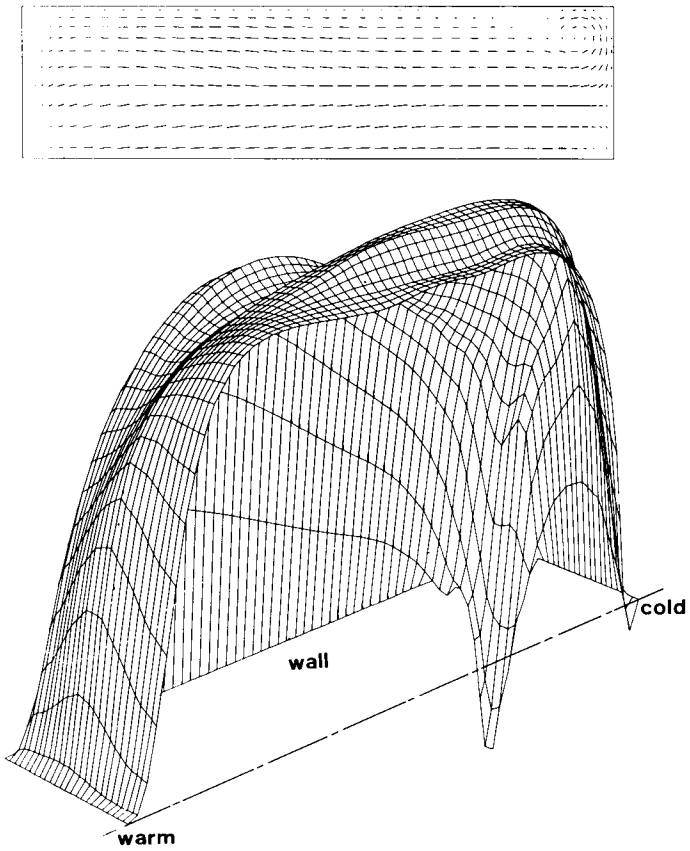


Figure 23. Velocity vectors on the free surface and perspective view of the axial velocity component; cylindrical crucible at $Gr = 300{,}000$

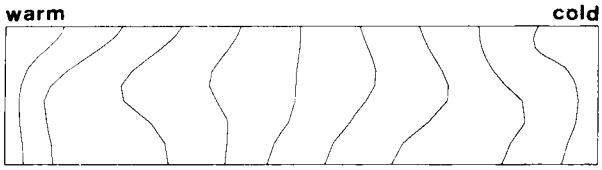


Figure 24. Isotherms at a depth equal to half the radius of the cylindrical crucible at $Gr = 300{,}000$

that the finite element mesh allows for the natural boundary condition on the plane of symmetry to be well satisfied.

Finally, Figure 24 shows the isotherms at a depth equal to half the radius of the crucible. The distorted shape of the isotherms leads us to expect skew liquid–solid interfaces in the actual growth process.

## 8. CONCLUSIONS

Our calculations show that three-dimensional effects can indeed be very important in the Bridgman growth process; the path lines are definitely not coplanar and the isothermal surfaces are curved in the $z$-direction.

We have not found in three dimensions the multicellular pattern which we had calculated for two-dimensional flows. In future work, we will investigate the reason why the iterative technique loses its convergence at high values of $Gr$. In particular, a transient analysis will be useful for detecting the occurrence of a periodic flow.

### ACKNOWLEDGEMENTS

S. Dupont and J. M. Marchal wish to acknowledge a scholarship from the Belgian 'Fonds National de la Recherche Scientifique'.

### REFERENCES

1. M. J. Crochet, F. T. Geyling and J. J. Van Schaftingen, 'Numerical simulation of the horizontal Bridgman growth. Part I: two-dimensional flow', *Int. j. numer. methods fluids*, **7**, 29–47 (1987).
2. D. T. J. Hurle, E. Jakeman and C. P. Johnson, 'Convective temperature oscillations in molten gallium', *J. Fluid Mech.*, **64**, 565–576 (1974).
3. J. E. Hart, 'Stability of thin non-rotating Hadley circulations', *J. Atmos. Sci.*, **29**, 687–697 (1972).
4. A. E. Gill, 'A theory of thermal oscillations in liquid metals', *J. Fluid Mech.*, **64**, 577–588 (1974).
5. G. D. Mallinson and G. de Vahl Davis, 'Three-dimensional natural convection in a box: a numerical study', *J. Fluid Mech.*, **83**, 1–31 (1977).
6. R. L. Sani, P. M. Gresho, R. L. Lee and D. F. Griffiths, 'The cause and cure (?) of the spurious pressures generated by certain FEM solutions of the incompressible Navier–Stokes equations: Part 1', *Int. j. numer. methods fluids*, **1**, 17–43 (1981).